

# Photocatalytic Removal of Toluene with CdIn<sub>2</sub>S<sub>4</sub>/CNFs as Catalyst: Effect of Ozone Addition

Run Yu Liu

National Central University

Minh Man Trinh

National Central University

Moo-Been Chang (✉ [mbchang@ncuen.ncu.edu.tw](mailto:mbchang@ncuen.ncu.edu.tw))

National Central University

---

## Research

**Keywords:** CdIn<sub>2</sub>S<sub>4</sub>/CNFs, Photodegradation, toluene, Ozone enhanced photocatalytic oxidation

**Posted Date:** August 17th, 2021

**DOI:** <https://doi.org/10.21203/rs.3.rs-688592/v1>

**License:** © ⓘ This work is licensed under a Creative Commons Attribution 4.0 International License.

[Read Full License](#)

---

**Version of Record:** A version of this preprint was published at Sustainable Environment Research on January 24th, 2022. See the published version at <https://doi.org/10.1186/s42834-022-00117-y>.

Photocatalytic removal of toluene with CdIn<sub>2</sub>S<sub>4</sub>/CNFs as catalyst: effect of ozone addition

Run Yu Liu<sup>1</sup>, Minh Man Trinh<sup>1</sup>, Moo Been Chang<sup>1\*</sup>

<sup>1</sup>: Graduate Institute of Environmental Engineering, National Central University, Chungli, Taiwan

\*Corresponding author **E-mail address:** mbchang@ncuen.ncu.edu.tw.

## **ABSTRACT**

CdIn<sub>2</sub>S<sub>4</sub> (CIS) has attracted much attention in the photocatalysis research field due to its structural stability and photoelectric properties. However, it's difficult to recycle when after usage, so application of CIS photocatalysis in removing volatile organic compounds (VOCs) is still limited and the literature on applying carbon nanofibers (CNFs) as electron acceptor is scarce. In this study, a novel CIS/CNFs composite was synthesized via a simple hydrothermal method. X-ray diffraction (XRD), Scanning electron microscope (SEM) and X-ray photoelectron spectroscopy (XPS) were applied to characterize the structure, microtopography and composition of CIS/CNFs photocatalyst prepared. The results showed that CNFs with the size of about 300 nm were favorable connected with CIS to form 3D conductive network and CIS particles with the average size of 100 nm grew onto the surface of CNFs uniformly. Results of photocatalytic degradation tests indicate that under visible light irradiation, degradation of toluene reached the optimal level of 86% as the CIS doped with 3% CNFs. It proved that the composite material prepared had an excellent photocatalytic recycle efficiency via repeated experiments. Furthermore, 95% removal efficiency was achieved as 200 ppm ozone was added into the system and mineralization rate are also improved. Derived from the intermediates detected, possible pathways of toluene degradation were proposed. Hence, this study presents a new method to synthesize photocatalyst with visible-light driven ozone-enhanced photocatalysis process toward indoor air pollutants removal VOCs.

Keywords: CdIn<sub>2</sub>S<sub>4</sub>/CNFs, Photodegradation, toluene, Ozone enhanced photocatalytic

oxidation

## 1.Introduction

Along with the continuous progress of industrialization and enhancement standard of living, excessive amounts of volatile organic compounds (VOCs) have been used and released from indoor decoration and other aspects [1]. Long-term exposure to VOCs may lead to influence of human body respiratory system and urinary system [2]. Indoor toluene has the characteristics of wide source, low concentration and long duration [3]. Traditional methods for removing VOCs include adsorption [4] and condensation [5], but secondary pollution may occur. Thermal catalytic oxidation [6], non-thermal plasma [7] and photocatalysis [1] have been proved to be effective for VOCs removal. However, low mineralization rate, high energy consumption and deactivation of catalyst are the disadvantages. To solve the bottleneck, combination of above techniques to treat VOCs containing gas streams has recently gained much attention [8-10].Ozone-enhanced photocatalytic oxidation (O<sub>3</sub>-PCO) is one of the promising VOCs control technologies [11, 12]. The recent studies found that introduction of ozone not only improves the performance of photocatalytic oxidation, but also facilitates catalyst regeneration [13]. Therefore, in order to improve the efficiency of ozone-enhanced photocatalytic oxidation, which is essential to develop stable structure and excellent properties photocatalyst.

CdIn<sub>2</sub>S<sub>4</sub> (CIS) is a ternary n-type chalcogenide with superior thermal stability and unique photoelectric properties; for instance, narrow band gap (2.0 eV) and large specific surface area which benefit the rapid excitation of charge carriers due to

effective absorption of visible light [14-16]. CIS is more stable than CdS which suffer from serious photo-corrosion under illumination due to the presence of  $\text{In}^{3+}$  along with  $\text{Cd}^{2+}$  ions [17, 18]. However, powdered materials are difficult to recycle after dispersion, which limits their application in the real environment [19].

Carbon nanofibers (CNFs) as a suitable electron acceptor can inhibit the secondary recombination of electron holes due to its superior electron transport behavior, stable physicochemical properties and high adsorption capacity [20-23]. Zhang et al. [24] adopted nano-carbon fiber to support metal gold ions and compounded them with  $\text{In}_2\text{S}_3$ . The results indicate that the photocatalytic activity was enhanced due to the network structure of composite nanofiber, and the degradation efficiency of Rhodamine B was greatly improved. At the same time, combination of CNFs with catalyst effectively solves the defects such as photo-corrosion. Wang et al. [25] and Zhang et al. [26] synthesized  $\text{Bi}_2\text{WO}_6/\text{CNFs}$  composite material by pairing  $\text{Bi}_2\text{WO}_6$  with CNFs. The results showed that heterogeneous structure was formed between the composite materials and there was a strong interaction, leading to enhanced photocatalytic activity. Moreover, due to the three-dimensional (3D) network structure, adding CNFs enhances the electron transmission as well as facilitates the recovery and reuse of the catalyst [24, 27]. Therefore, it could expect that coupling CIS with electrospun CNFs to prepare CIS/CNFs would inhibit the electron-hole pair recombination to bring about enhanced photoactivity and regeneration of catalyst.

In this study, the CIS/CNFs photocatalytic material was synthesized by hydrothermal method. The physical and chemical structures of photocatalysts prepared

were investigated by scanning electron microscopy (SEM), transmission electron microscopy (TEM), X-ray diffraction (XRD) and X-ray photoelectron spectroscopy (XPS). Photoluminescence (PL) was used to investigate the photoelectric properties of the samples. The catalytic ability of the CIS/CNFs materials for the degradation of toluene was evaluated under visible light, and ozone-enhanced photocatalysis oxidation was applied to improve the removal efficiency. Through the analysis of the experimental data, a viable catalytic pathway for the degradation of pollutants by the materials prepared was explored and discussed. This study provides a new high-performance catalyst for degrading toluene.

## 2. Materials and Methods

### 2.1 Chemicals and materials.

In this study, all reagents were of analytical-grade and used as received. Reagents used include: deionized water, indium nitrate  $\text{In}(\text{NO}_3)_3 \cdot 4.5\text{H}_2\text{O}$  (Sinopharm Chemical Reagent Co. Ltd.), cadmium nitrate tetrahydrate  $\text{Cd}(\text{NO}_3)_2 \cdot 4\text{H}_2\text{O}$  (Sinopharm Chemical Reagent Co. Ltd.), carbon Nano-fibres (Sinopharm Chemical Reagent Co. Ltd.), sodium sulfide ( $\text{Na}_2\text{S} \cdot 9\text{H}_2\text{O}$ ) (Sinopharm Chemical Reagent Co. Ltd.), nitric acid ( $\text{HNO}_3$ ), toluene (analytical reagent, Xilong Chemical Co., Ltd.) and anhydrous alcohol (analytical reagent, Xilong Chemical Co., Ltd.).

### 2.2 Synthesis of CIS and CIS-CNFs composites

The CIS and CIS/CNFs were synthesized by simple hydrothermal method, with analytical-grade  $\text{In}(\text{NO}_3)_3 \cdot 4.5\text{H}_2\text{O}$ ,  $\text{Cd}(\text{NO}_3)_2 \cdot 4\text{H}_2\text{O}$  and  $\text{Na}_2\text{S} \cdot 9\text{H}_2\text{O}$  as raw material. Stoichiometric amounts of  $\text{In}(\text{NO}_3)_3 \cdot 4.5\text{H}_2\text{O}$ ,  $\text{Cd}(\text{NO}_3)_2 \cdot 4\text{H}_2\text{O}$  and  $\text{Na}_2\text{S} \cdot 9\text{H}_2\text{O}$  were dissolved in deionized water under ultrasonication to obtain homogeneous solution. After dissolution, place the solution in a beaker with a magnetic stirrer. During the stirring process, indium nitrate hydrate and cadmium nitrate hydrate are slowly dropped into the sodium sulfide solution until a uniform pale-yellow sol is formed. Finally, the mixed solution was kept at  $100^\circ\text{C}$  for 18 h in a Teflon-lined autoclave for continuous hydrothermal reaction, and then cooled to room temperature. The slurry was recovered by filtration, washed with deionized water and dried at  $120^\circ\text{C}$  overnight.

For the CIS/CNFs preparation, CNFs was mixed with analytical-grade  $\text{In}(\text{NO}_3)_3 \cdot 4.5\text{H}_2\text{O}$ ,  $\text{Cd}(\text{NO}_3)_2 \cdot 4\text{H}_2\text{O}$  and  $\text{Na}_2\text{S} \cdot 9\text{H}_2\text{O}$ , and the subsequently preparation steps were similar to  $\text{CdIn}_2\text{S}_4$  as reported earlier. The samples are denoted as CIS/CNFs wt% based on the loading of CNFs, named as CIS/CNFs-1, CIS/CNFs-2, CIS/CNFs-3 and CIS/CNFs-4, respectively.

### 2.3 Catalyst characterization

### 2.3 Catalyst characterization

BET surface area and pore volume of catalysts were determined by nitrogen adsorption (Micromeritics ASAP 2020, USA). The crystal structure of the as-synthesized CIS/CNFs by hydrothermal method was determined by Bruker X-ray diffractometer (D8-Advance, Germany) using Cu-K $\alpha$  radiation. Data was collected at scan rate of 0.02° s<sup>-1</sup> and from 10° to 80° (2 $\theta$ , diffraction angle). High-resolution transmission electron microscopy (HRTEM) micrographs were obtained with a Tecnai G2 F20 S-TWIN microscope and operated at 200 kV. Scanning electron microscope (SEM) images of the catalysts were obtained on a Nova NanoSEM 450 microscope operated at 200 kV. X-ray photoelectron spectroscopy (XPS) analyses were performed on a Thermo Fisher Scientific ESCALAB 250 photoelectron spectrometers. Photoluminescence (PL) spectra was carried out on a spectrometer with an excitation wavelength of 325 nm (Varian Cary Eclipse, America). Photocurrent responses was observed by electrochemical workstation (CHI 660B).

#### 2.4. Photocatalytic tests

Catalytic degradation of toluene was tested in a self-designed reactor at room temperature. The experimental setup is shown in Fig. 1. The volume of dark organic-glass reactor is 0.5 L. Prior to each experiment, 50 mg photocatalyst powder was uniformly dispersed in 20 mL ethanol solution and then coated on a round glass plate with a diameter of 5 cm, placing the sample-coated dishes in the bottom of reactor with a glass slide cover. After that, the standard gas (60 ppm toluene in air) was passed into

the reactor. The reactor was kept in the dark condition for 1 h to achieve an equilibrium of adsorption and desorption. The initial toluene concentration was remained at 60 ppm after adsorption equilibrium. The glass slide cover on the petri dish was then removed to begin the catalytic oxidation of toluene. Xenon lamp (MAX-350, Nmerry Technology.Co) occluded by a fixed wavelength filter produces a visible light source. Reaction in light condition for 3.5 h. The sample was collected and then injected by a sampling probe into the gas chromatograph (GC) for measurement. The analysis of CO<sub>2</sub>, CO, and water vapor was conducted online with a Photoacoustic IR Multigas Monitor (INNOVA air Tech Instruments, Model 1412). As for the ozone-enhanced photocatalysis experiment, ozone with a concentration of 200 ppm (about 1 L) was fed into the reactor and the above experimental steps were repeated. The ozone concentration was monitored by an ozone detector (OS50, Osenger Technology). The degradation tests were repeated for three times and low deviations (less than 10%) were observed.

The toluene removal efficiency was calculated by the following equation:

$$\text{Toluene removal efficiency} = \frac{\text{Toluene}_{\text{initial}} - \text{Toluene}_{\text{final}}}{\text{Toluene}_{\text{initial}}} \times 100\% \quad (\text{Eq.1})$$

where  $\text{Toluene}_{\text{initial}}$  and  $\text{Toluene}_{\text{final}}$  are the initial and final concentrations of toluene (ppmv), respectively.

The ozone utilization rate was calculated by the following equation:

$$\text{Ozone utilization rate} = \frac{\text{Ozone}_{\text{initial}} - \text{Ozone}_{\text{final}}}{\text{Ozone}_{\text{initial}}} \times 100\% \quad (\text{Eq.2})$$

where  $\text{Ozone}_{\text{initial}}$  and  $\text{Ozone}_{\text{final}}$  are the initial and final concentrations of ozone (ppmv), respectively.

The toluene mineralization rate was calculated by the following equation:

$$\text{Toluene mineralization rate} = \frac{\text{CO}_{2\text{final}}}{7 \times \text{Toluene}_{\text{initial}}} \times 100\% \quad (\text{Eq.3})$$

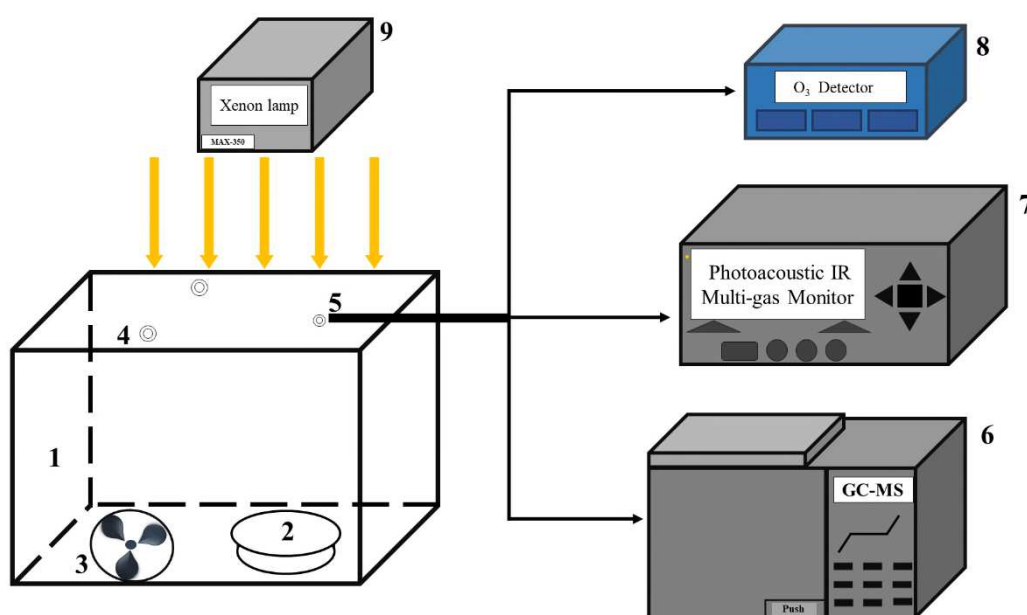


Fig.1 Schematic of experimental set-up for ozone-enhanced photocatalysis oxidation of toluene: (1) glass reactor, (2) glass petri dish coated with catalyst, (3) fan, (4) injection ozone and toluene port, (5) sampling port, (6) GC-MS, (7) Photoacoustic IR Multi-gas Monitor, (8) Pump-suction ozone detector, (9) Xenon lamp light source.

## 2.5 GC-MS heating program

Determination of intermediates and products produced after toluene degradation reaction by gas chromatography coupled with mass spectrometer (GC-MS) (Agilent

Technologies, America). Data was collected at temperature program on 35 °C for 10 min and rose to 125 °C at a rate of 5 °C per minute under column HP-5MS (30 m × 0.250 mm).

### 3. Results and discussion

#### 3.1 Photocatalytic performance

In order to determine the optimal dose of CIS/CNFs, experiments with various materials including CNFs doped with different percentage CIS are conducted. In the preliminary experiment, it's found that the degradation efficiency of toluene achieved with CIS/CNFs was lower than pure CIS materials when the CNFs content is  $\geq 5\%$  under the same conditions. We speculate that when too much CNFs is doped, some pores might be blocked due to the high dispersability of CNFs and the active sites of CIS would also be reduced as a result of reduced specific surface area. Therefore, 4% is chosen as the maximum doping rate of CNFs.

All degradation tests were conducted for three times and low deviations (less than 10%) were observed. Fig. 2(a) shows the adsorption of toluene on six groups of samples under dark conditions, indicating that all samples reach the equilibrium of adsorption and desorption after 30 minutes. Moreover, the pure carbon nanofibers have a high adsorption capacity possibly due to the 3D network structure. As the CNFs content

increases, CIS/CNFs adsorption capacity increases and it will combine with toluene molecules more closely, thus improves the photocatalytic degradation ability.

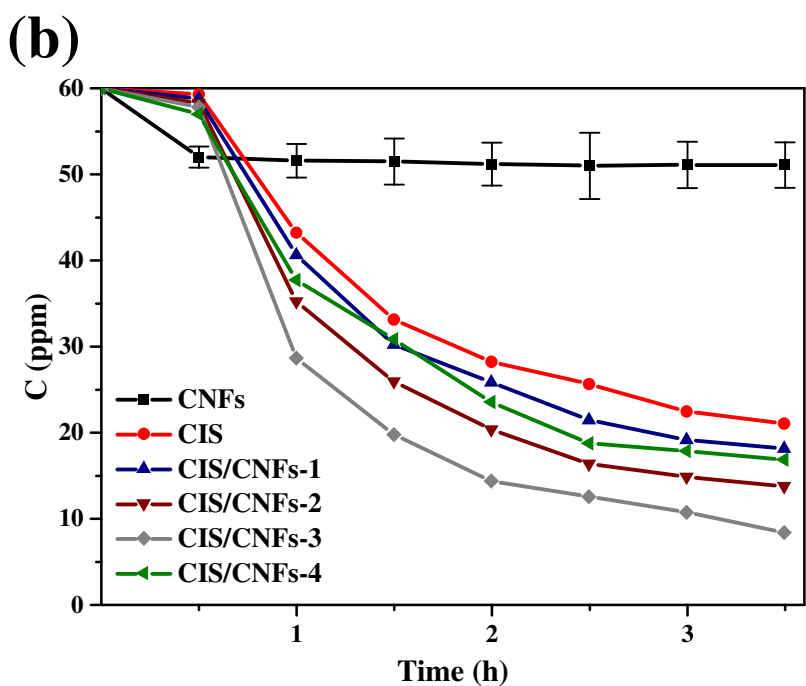
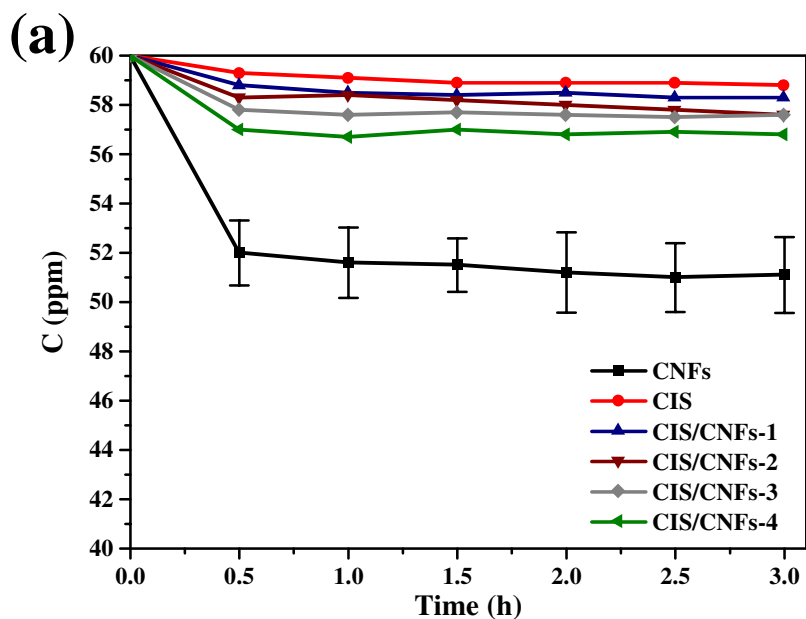


Fig. 2(a) Adsorption of toluene on CNFs and CIS; (b) Degradation of toluene achieved with CNFs, CdIn<sub>2</sub>S<sub>4</sub> and CIS/CNFs with different percentage.

As can be seen from Fig. 2(b), when the doping rate of CNFs is 3%, the photocatalytic degradation of toluene reached the optimal (86.1%) and as the doping rate increases to 4%, photocatalytic efficiency is reduced to 72%. As too much carbon nanofibers are added, carbon nanofiber may cover part of the CIS particles, to reduce light absorption and utilization. Results of toluene removal obtained in this study are summarized and compared with other studies under the same experimental protocol, as shown in Table 1. It can be observed that the performance of CIS/CNFs-3 prepared via simple hydrothermal method is comparable to those reported in literature over various catalysts.

### 3.2. Ozone-enhanced photocatalysis tests

#### 3.2.1 Toluene degradation performance and mineralization rate of different processes

Ozone is a powerful oxidizing agent which has been applied in a wide range of photocatalytic oxidation (PCO) to improve the performance. In this study, 200 ppm of ozone was introduced into the system to conduct ozone-enhanced photocatalytic oxidation (O<sub>3</sub>-PCO) tests of toluene with CIS, CNFs, and CIS/CNFs, respectively, as shown in Fig. 3.

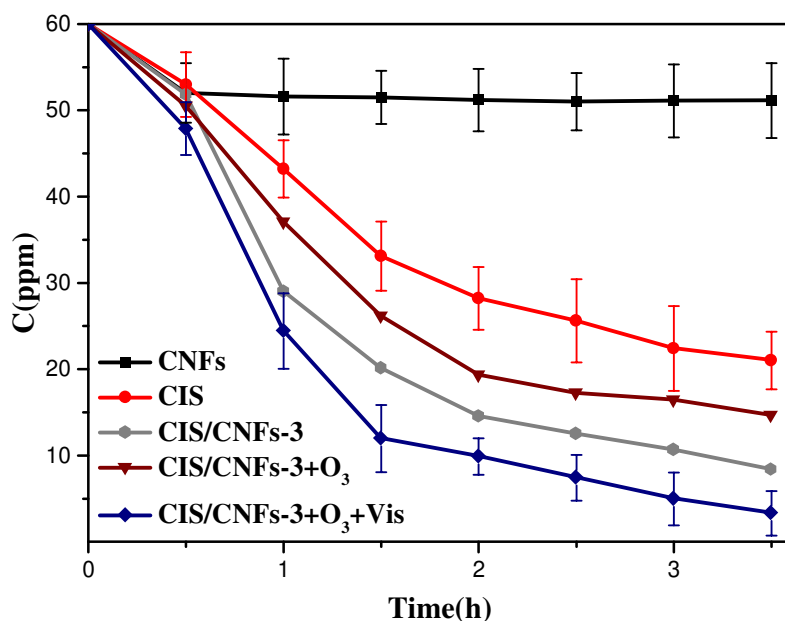


Fig. 3 Degradation of toluene achieved with performance different processes.

The experiment is divided into three processes, i.e., CIS/CNFs+Vis, CIS/CNFs +O<sub>3</sub> and CIS/CNFs +O<sub>3</sub>+Vis. Toluene degradation efficiencies achieved with CIS +Vis and CIS/CNFs +O<sub>3</sub> reach 86.1% and 75.6%, respectively. After ozone is injected, the efficiency of PCO system increases significantly to 95%.

In the meantime, the introduction of ozone significantly improves the mineralization rate of toluene, indicating that ozone and PCO system had excellent synergistic sequence. For photocatalyst tests, the photocatalyst gradually became deactivated after being operated for specific sometimes, which may be caused by the adhesion of intermediates produced in the degradation process of toluene to the surface of the catalyst, resulting in the blocking of the active sites on the catalyst surface and

the oxygen vacancy. However, the situation is greatly improved for O<sub>3</sub>-PCO, showing a slow upward trend throughout the process. Therefore, the introduction of ozone can improve the durability of catalysts, because catalyst deactivation is inhibited to some extent. As shown in Fig. S1, toluene mineralization rates of 87.3% and 76.8% and ozone utilization rates of 84.9% and 69.5% are achieved with CIS/CNFs+O<sub>3</sub>+Vis and CIS/CNFs+O<sub>3</sub>, respectively. It indicates that O<sub>3</sub>-PCO has the optimal toluene mineralization rate and ozone consumption rate in two methods, and toluene mineralization rate is positively correlated with ozone consumption rate. The mineralization rate of toluene is affected to some extent by the ozone consumption rate, but it is not completely dependent on the latter. Meanwhile, in CIS/CNFs+O<sub>3</sub>+Vis, the ozone utilization rate is over 80%, indicating that ozone is well consumed and utilized.

### 3.2.2 Influence of relative humidity on ozone-enhanced photocatalysis

In order to explore the influence of relative humidity on the performance of O<sub>3</sub>-PCO system, the gas streams with various relative humidity including 20%, 40% and 80%, respectively, were introduced into the system with CIS/CNFs-3 as catalyst for tests (Fig. S2). The results show that when the relative humidity is increased from 20% to 80%, removal rate of toluene increases from 60% to 95%, and there exists a positive correlation. As the relative humidity is increased, more water vapor can participate in the photocatalytic reaction, thus generating more hydroxyl radicals with strong oxidability, thereby the removal efficiency of toluene is improved.

In brief, the above experimental result confirmed the photocatalytic activity of CIS/CNFs and showed 95% degradation activity for toluene. At the same time, introduction of ozone into the system not only improved the photocatalytic efficiency, but also increased toluene mineralization rate. In the preliminary experiment, investigated the influence of different concentrations of ozone on the photocatalytic oxidation of toluene. Unfortunately, with the increase of ozone concentration, the ozone utilization rate was decreased, so 200ppm was chosen as the experimental ozone concentration.

### 3.2.3 Kinetic analysis

Fig. S3 shows the relationship between  $\ln(C_0/C)$  and T by fitting the first-order reaction kinetic equation. When 3% CNFs were doped into CIS,  $K_{app}$  for toluene degradation reaches  $0.407\text{ h}^{-1}$ , which was greater than pure CIS ( $0.279\text{ h}^{-1}$ ). It follows that CIS/CNFs composite material has a higher photocatalytic activity, and the toluene degradation reaches the optimal level when 3% CNFs is doped. In order to confirm the advantages of catalytic degradation of toluene, the characteristics of BET, XRD, XPS and SEM to analyzed in the following sections.

## 3.3. Characterizations of photocatalytic materials

### 3.3.1 BET analysis of CIS

The N<sub>2</sub> sorption isotherms of CIS and CIS/CNFs-3 showed type III character with a well-developed and distinct hysteresis loop (Fig. S4). The BET analysis of CIS material and CIS/CNFs-3 composite material indicates that specific surface areas of CIS and CIS/CNFs-3 composite material are 38.6 m<sup>2</sup> g<sup>-1</sup> and 43.3 m<sup>2</sup> g<sup>-1</sup>, respectively. As CNFs is doped, the specific surface area of CIS material is enhanced, a larger specific surface area can expose more surface active sites, which is favorable for the adsorption of toluene and ozone, so the photocatalytic degradation of toluene is also improved.

### 3.3.2 Crystalline structures

The crystal structure and phase properties of CNFs, CIS, and CIS/CNFs samples with various doping contents were investigated by XRD pattern and the results as in Fig. 4. From Fig. 4, the six well-defined characteristic diffraction peaks at  $2\theta=23.18^\circ$ ,  $27.25^\circ$ ,  $33.00^\circ$ ,  $43.32^\circ$  and  $47.41^\circ$  can be consistent with the (220), (311), (400), (511) and (440) planes of the cubic crystal lattice with a spinel structure of CIS (JCPDS 270060), respectively. As for CNFs, the first wide peak at  $2\theta=25.0^\circ$  is corresponding to (002) crystal plane. The sharp and strong diffraction peak of pure CIS indicates that the sample has good crystallinity. As CIS nanoparticles were grown on the carbon fiber surface, the XRD patterns of all CIS/CNFs composites were similar to those of pure CIS materials. The peak in the (311) plane of CIS/CNFs composite material was

compared with that of pure CIS as shown in Fig. 2(b), and an obvious shift to lower  $2\theta$  values was observed, which may be caused by the strong interaction between CIS and CNFs. Meanwhile, with the increase of CNFs doping content, the deviation of the peak become more intensive. In addition, it was observed that CIS diffraction peaks was broadened and weakened in intensity as 3% carbon fiber was doped. This indicates that doping CNFs is not conducive to CIS crystallinity, the catalyst with poor crystallinity generates more surface defects in the catalyst structure, which is favorable to the adsorption and decomposition of toluene and ozone molecules [28]. A high defect density is conducive to the adsorption of ozone molecules on the surface of the catalyst [29]. The average grain size ( $D$ ) of the catalysts can be calculated from the line broadening of XRD peaks using Scherrer's formula [30].

$$D = K \lambda / (\beta \cos \theta) \quad (\text{Eq.4})$$

where  $K$  is a constant (0.89);  $\lambda$  is the wavelength of the X-ray radiation (Cu  $K\alpha=0.1541$  nm);  $\beta$  is the full width at half-maximum and  $\theta$  is the angle at position of peak maximum [31]. The as-calculated grain size of monomeric CIS is 27.5 nm, while the grain sizes of series composites CIS/CNFs are 25.6 nm. In general, particle of smaller grain size has a larger specific surface area [29]. What's more, the grain sizes also imply that CIS/CNFs are favorable to the adsorption of toluene and ozone at defect sites. This result was also supported by the data obtained by BET analysis. The above results indicate that CIS/CNFs composite material was successfully synthesized and CIS was not destroyed during the process of CNFs growth.

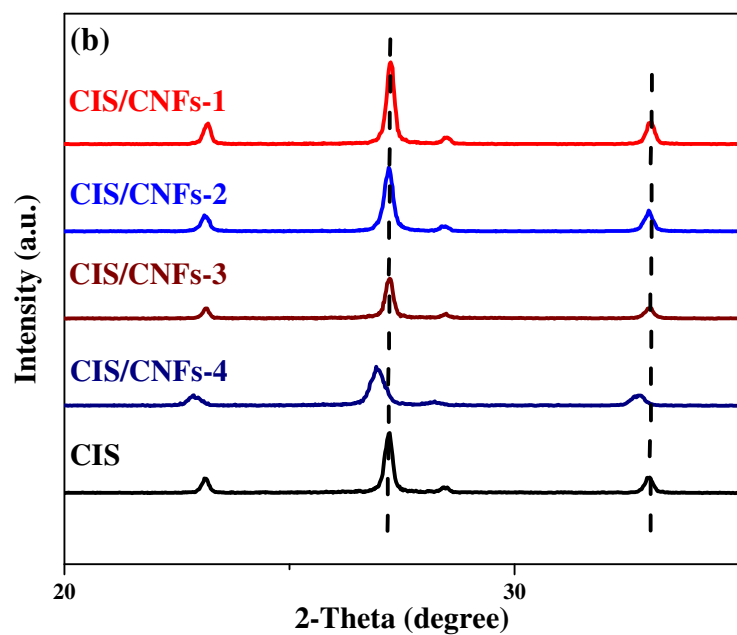
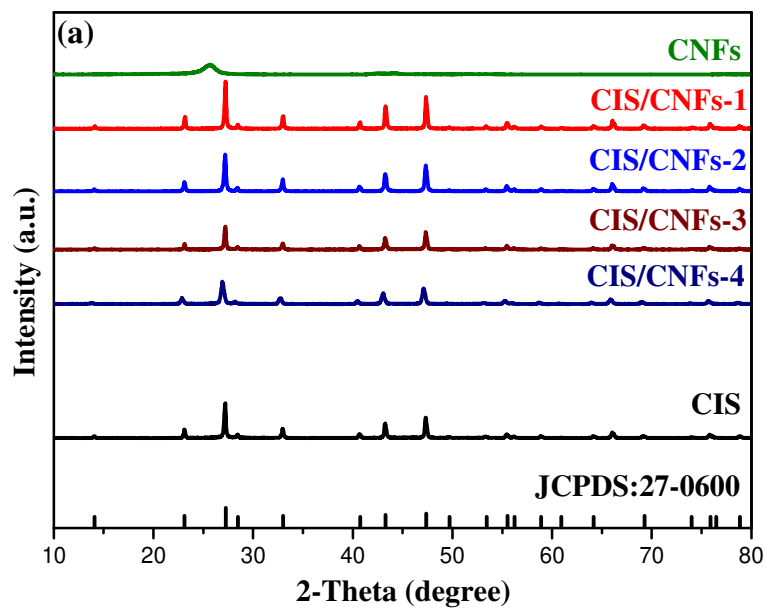


Fig. 4(a) XRD patterns of CIS, CNFs and CIS/CNFs heterojunctions (CIS/CNFs-1, 2, 3 and 4); (b) the magnified XRD patterns of CIS and CIS/ CNFs-x nanocomposites.

### 3.3.3 Morphology of CIS/CNFs photocatalyst

The morphology of the sample is analyzed by SEM and TEM, as shown in Fig. 5. The diameter of carbon nanofibers is about 300 nm and the lengths are up to several microns. It has a high aspect ratio, and the surface is smooth and closely connected to form a 3D conductive network, which is beneficial to the transmission of electrons generated during light irradiation. The SEM image of CIS is shown in Fig. 5(b), indicating that the CIS particles have 3D octahedral shape, and the illustration clearly shows that CIS octahedral particles have good crystal faces. In addition, as shown in Fig. 5(c), via hydrothermal reaction, CIS particles grow evenly on the carbon nanofibers, forming CIS/CNFs composite materials. There is no obvious aggregation phenomenon in the SEM images of CIS/ CNFS composites.

Fig. 5(d) reveals that octahedral CIS has a clear interface, with the particle size of about 100 nm. At the same time, it can be found in Fig. 5(e) that via hydrothermal synthesis of CIS/CNFs composite materials, the crystal structure of CIS nanomaterial remains intact and tightly bound to carbon fiber. Fig. 5(f) shows the HRTEM image of CIS/CNFs composite material, exhibits a distinct visible lattice fringe of 0.338 nm, which corresponding to the (002) plane of CNFs. The lattice fringes have distance of 0.626 nm and 0.327 nm corresponding to (111) and (311) planes of CIS, respectively, indicating that the hydrothermal synthesis of CIS/CNFs composite material does not destroy the microscopic morphology of CIS crystal. In conclusion, CIS and CNFs were successfully coupled to form composite material and CIS was not destroyed during the growth process of CNFs, which is consistent with the results of SEM observations.

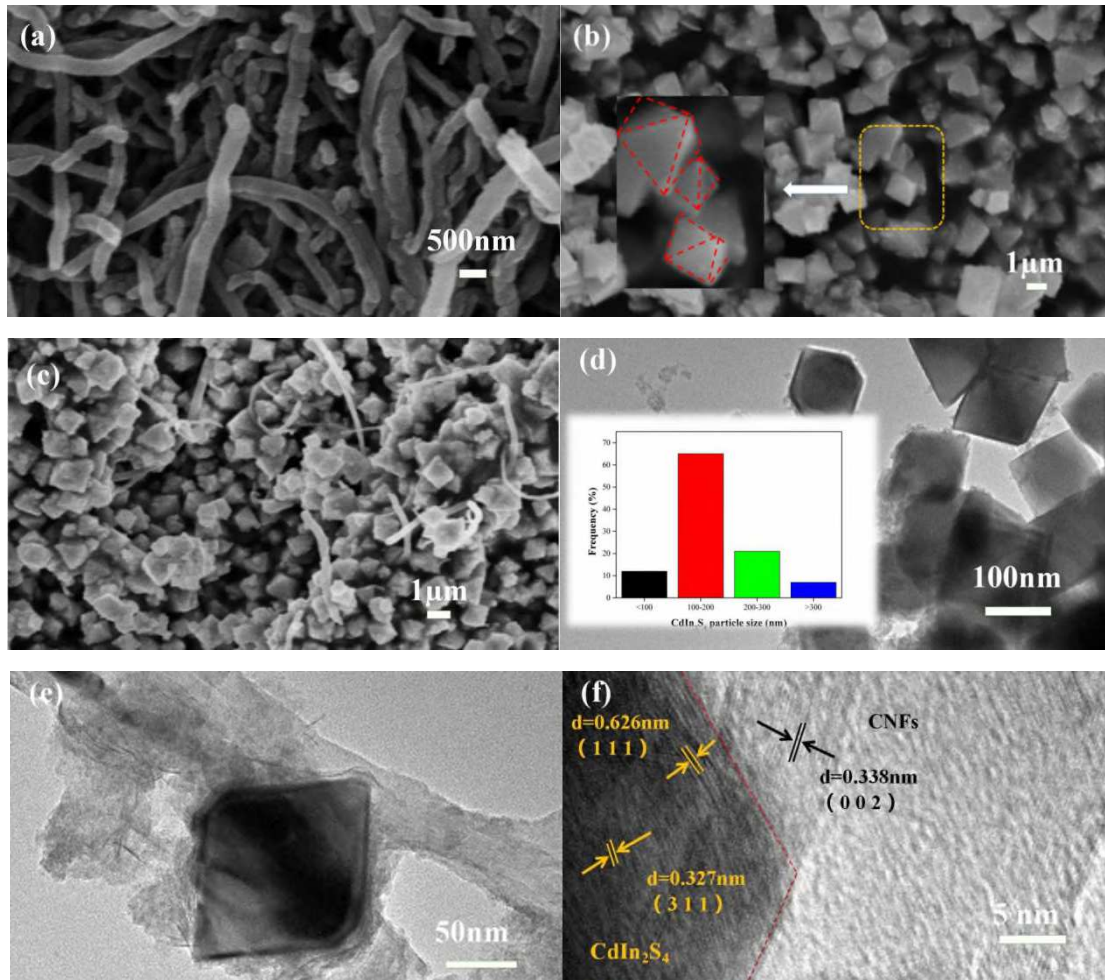
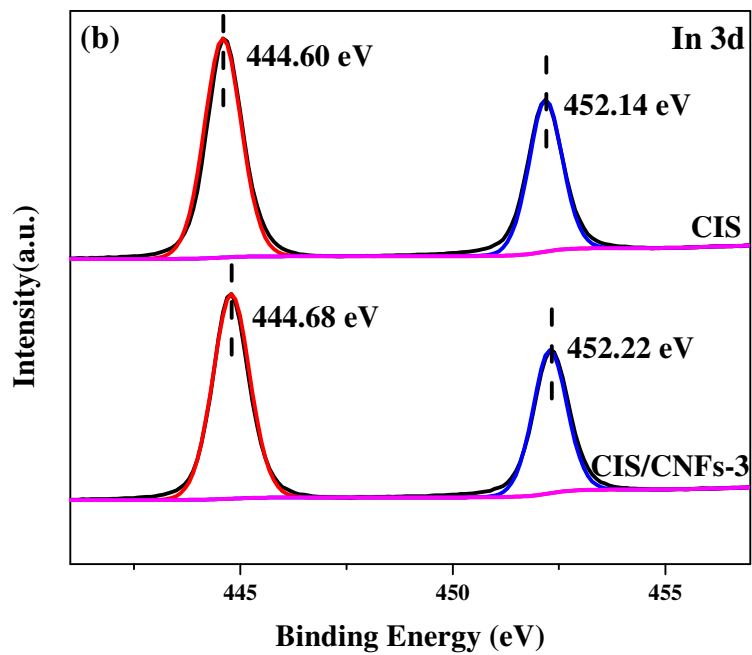
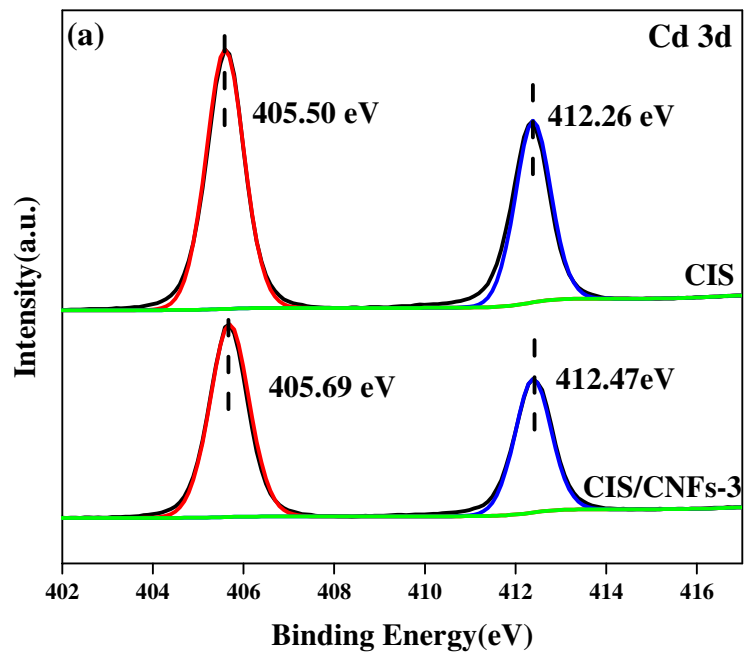


Fig. 5 Representative FESEM images of (a) pure CNFs, (b) CIS and (c) CIS/CNFs-3; (d) TEM images of pure CNFs, (e) TEM images of CIS/CNFs-3, (f) HRTEM images of CIS/CNFs-3.

### 3.3.4 Structure and composition of CIS/CNFs photocatalyst

The surface element states of the constituent elements in the CIS and CIS/CNFs nanocomposite samples were investigated by XPS spectra as shown in Fig. 6. The spectra reveal all of nanocomposite contain Cd, In, S, and C elements. The high-resolution XPS spectra of C 1s as shown in Fig. 6(d) and could be deconvoluted into

three peaks centered at 284.6 eV, 285.7 eV and 286.6 eV, respectively. The peak at 284.6 eV is attributed to C-C bond derived from amorphous carbon phase or indefinite carbon [32]. Peaks at 285.7 eV are characteristic of C-O groups. In addition, the weak peak at 286.6 eV was ascribed to carboxyl carbon (OC = O) [33, 34]. Fig. 6(a) showed the Cd 3d spectra could be deconvoluted into two peaks, the peaks at 405.5 and 412.26 eV were attributed to Cd 3d<sub>5/2</sub> and 3d<sub>3/2</sub> states, respectively, showing a normal state of Cd<sup>2+</sup> in sulfide environment [35]. As shown in Fig. 6(b), in the In 3d spectra, the peaks at 444.6 eV and 452.14 eV were respectively assigned to the 3d<sub>5/2</sub> and 3d<sub>3/2</sub> states when the In<sup>3+</sup> ion is coordination with the sulfide ion [16]. In Fig. 6(c), S 2p spectra were deconvoluted into two peaks at 161.31 eV and 162.49 eV, which were assigned to 2p<sub>3/2</sub> and 2p<sub>1/2</sub> levels of S<sup>2-</sup>, respectively [36]. In addition, the spin orbital splits of Cd 3d, In 3d, and S 2p in CIS and CIS/CNFs samples were 6.76 eV, 7.56 eV, and 1.18 eV, respectively, indicating that the valence states of Cd, In, and S in CdIn<sub>2</sub>S<sub>4</sub> and CIS/CNFs samples are Cd<sup>2+</sup>, In<sup>3+</sup>, and S<sup>2-</sup>, respectively. Compared with the pure CIS sample, the spin orbit of S 2p in the CIS/CNFs sample deviated and moved towards the direction of low binding energy, possibly due to strong interaction between two materials. Therefore, the XPS results further demonstrate that CIS and CNFs coexist in CIS/CNFs-3 composites, and CIS and CNFs are connected by chemical bonds, rather than simply mixing the two materials to form a mixture, and it turns out that carbon nanofibers have been successfully doped on the surface of CIS nano-octahedron. This result was also consistent with revealed by XRD patterns.



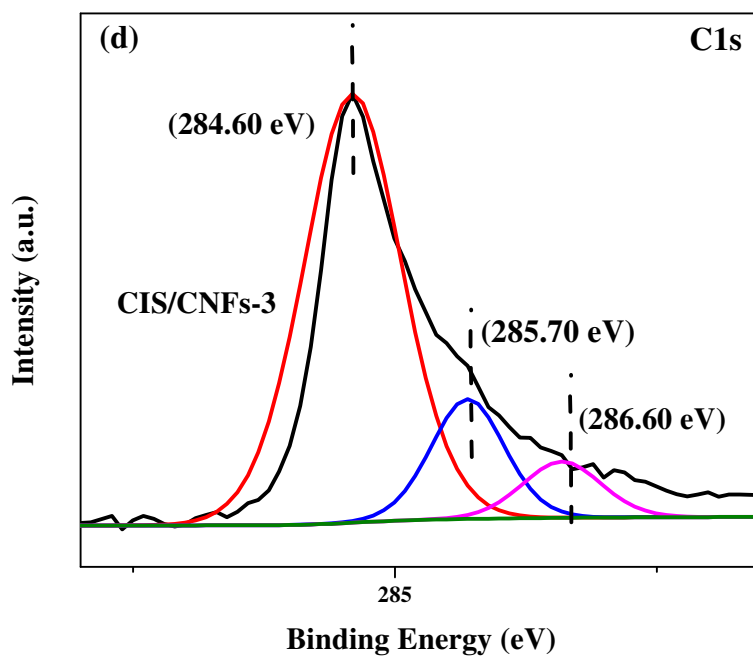
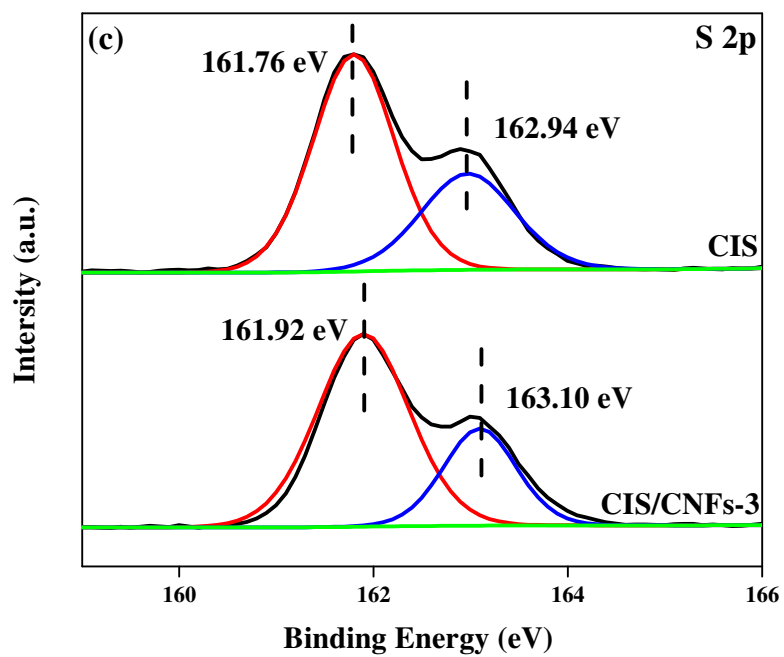


Fig. 6 XPS analysis of as-prepared CIS and CIS/CNFs-3: (a) Cd 3d; (b) In 3d; (c) S 2p; (d) C 1s.

### 3.4 Photo- and electro-chemistry performance

#### 3.4.1 Photochemical analysis

The photocurrent had been considered as an efficient method to estimate recombination rate of electron-hole pairs [37]. As shown in Fig. 7, the photocurrent spectrum was obtained by using xenon lamp as light source and  $\text{Na}_2\text{SO}_4$  as electrolyte.

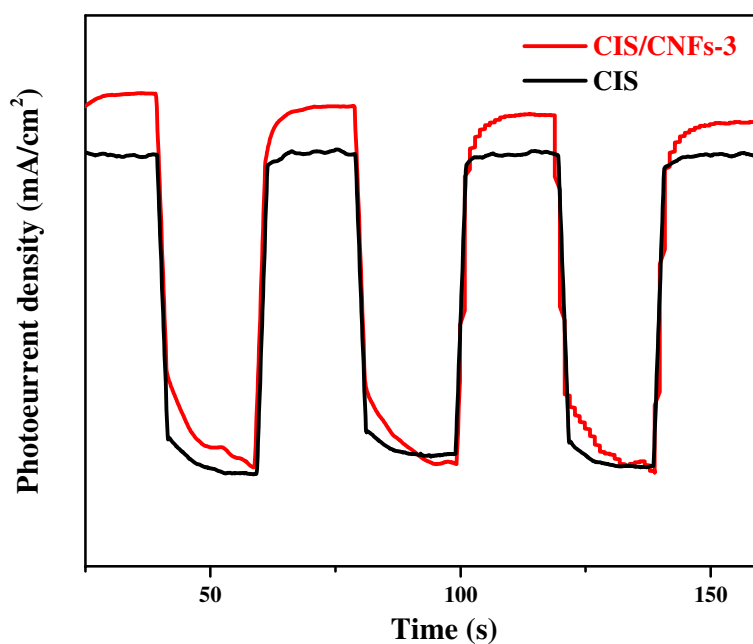


Fig. 7 Transient photocurrent response of CIS and CIS/CNFs-3 under irradiation

CIS and CIS/CNFs-3 show a repeatable photocurrent response under visible light irradiation, indicating that the samples prepared by hydrothermal method is stable. Owing to the poor absorption of visible light, CIS shows a low anodic photocurrent

$1.60909 \times 10^{-3} \mu\text{A cm}^{-2}$ . Compared with pure CIS, the CIS/CNFs-3 nanocomposite exhibits higher anodic photocurrent of  $1.6327 \times 10^{-3} \mu\text{A cm}^{-2}$ , which is 1.2% more than pure CIS. CIS/CNFs composite material reveals rapid transfer of interfacial charge, which can effectively inhibit the photogenic electron hole pair recombination and promote the efficient separation of photogenic carriers, so the photocurrent density of CIS/CNFs composite material tested under the same conditions is significantly greater than that of CIS. The result indicate that CIS and carbon nanofibers can effectively promote the separation of photogenerated charge carriers and inhibit the recombination rate of electron-hole pairs.

#### 3.4.2 PL spectra of CIS and CIS/CNFs-3 composites

Photoinduced electron-hole recombination causes negative impact on photocatalyst photodegradation activity and reduce the degradation efficiency of toluene, and the recombination rate of electron-hole is directly proportional to the photoluminescence (PL) intensity [38]. Therefore, PL spectra are used to study the degree of electron hole separation of these photocatalysts.

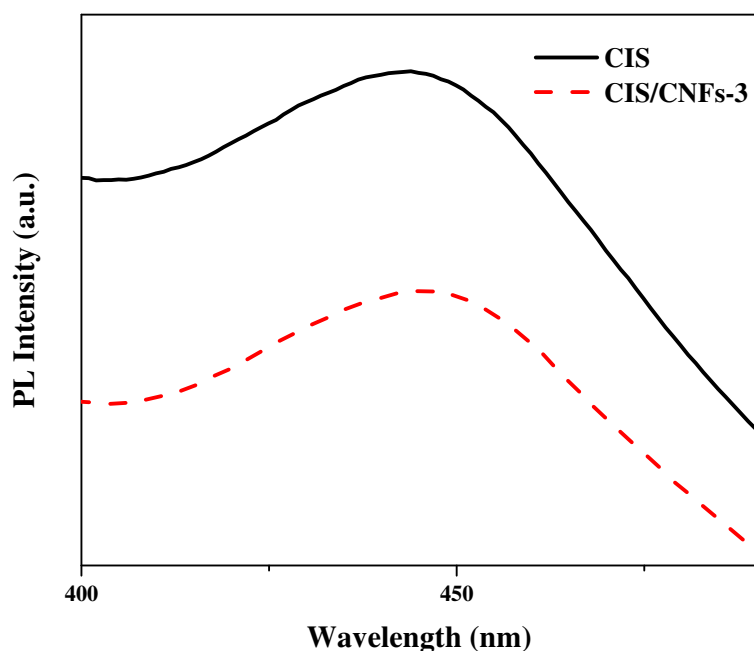


Fig. 8 PL spectra of CIS and CIS/CNFs-3 composites at room temperature

As shown in Fig. 8, due to rapid recombination of photogenerated electron-hole pairs, all samples are of corresponding characteristic emission peaks at approximately 445 nm. The PL intensity of CIS/CNF-3 was smaller than that of CIS, which was consistent with the results of electron-hole recombination. In contrast, CIS had the stronger emission peak, indicating that pure CIS had a faster electron-hole recombination process. Addition of CNFs resulted of the decrease in PL peaks.

The quenching of PL emission spectra of the CIS/CNFs can be attributed to efficient electron transfer between CIS and CNFs. Despite of the fact that CIS has a narrow band gap and a high spectral response range, visible light can be absorbed and utilized. However, due to the narrow band gap of CIS, electron-hole pairs are easy to recombine. On the other hand, the CIS/CNFs composite material can effectively inhibit

recombination of the electron–hole pairs and promote the efficient separation of photo-generated carriers due to rapid transfer of interfacial charge. As a result, the photocurrent density of CIS/CNFs composite material is significantly higher than that of CIS. It can be concluded that the addition of CNFs was beneficial to light absorption, effective photoelectron transfer between CIS and CNFs promotes the electron-hole pairs separation, thus improving the corresponding photocatalytic activity.

### 3.5 Photocatalytic recycling and stability of CIS/ CNFs

The stability of catalysts is of great importance to the successful application. In order to test the stability of CIS/CNFs-3 composite materials for ozone-enhanced photocatalysis, the catalyst was reused for 10 times, and each experiment was carried out under the same condition for three tests, and observed the XRD patterns before and after the use of the catalyst, as shown in Fig. 9.

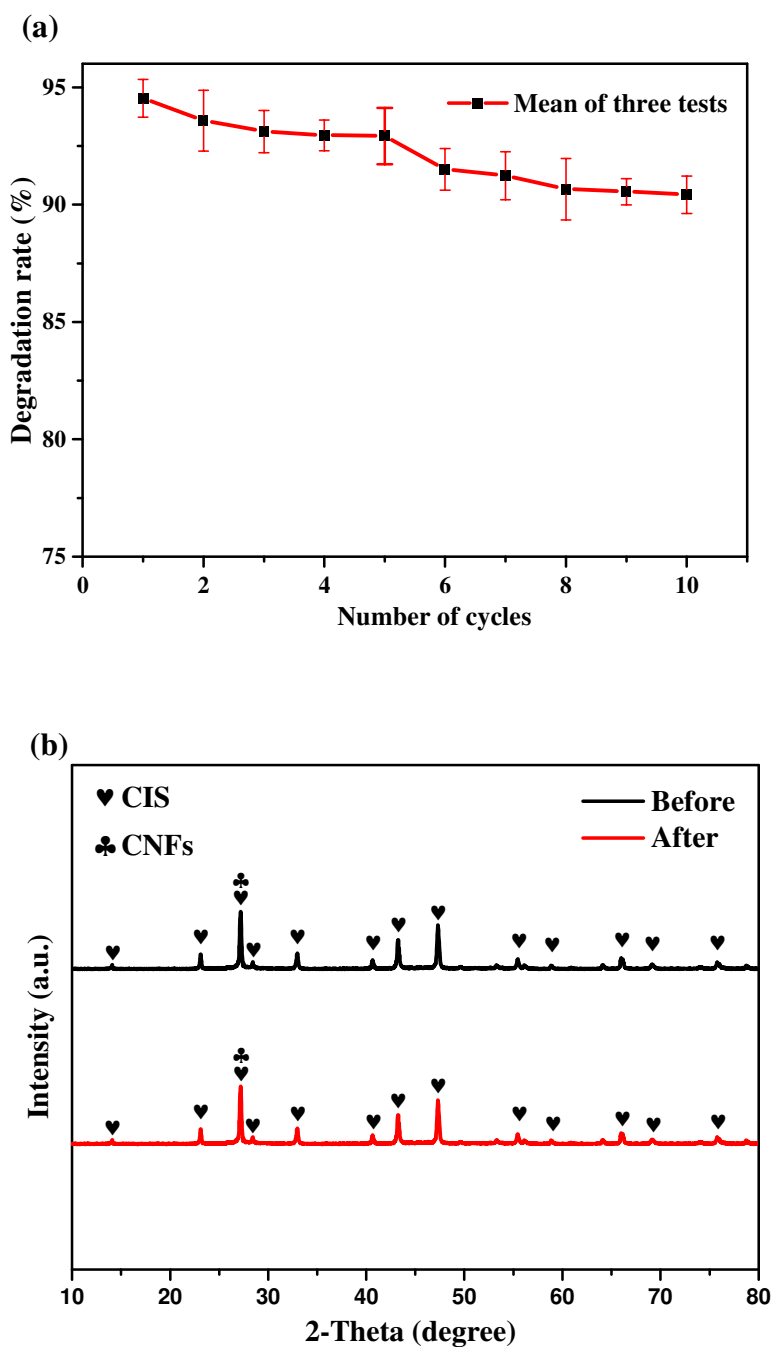


Fig. 9 (a) Degradation effect of recombination experiment; (b) XRD pattern of before and after 10 times repeated use.

Within ten cycles of the experiment, CIS/CNFs-3 composite material reveals low level of photocatalytic activity reduction, degradation efficiency decreases

slightly from 95% to 90.42% during 3 h tests, indicating that used sample still has good photocatalytic activity. The composite of carbon nanofibers can effectively inhibit the photo-corrosion and ozone corrosion. Fig. 9(b) shows the XRD pattern of CIS/CNFs-3 composite before and after XRD pattern of before and after 10 times repeated use. After 10 times reactions, the peak position and ratios were almost unchanged compared with the fresh photocatalyst. The results proved that the micro-morphology of the photocatalyst did not change after the 10 times repeated tests, indicating that CIS/CNFs-3 has significant stability for ozone-enhanced photocatalysis.

### 3.6 Possible degradation mechanisms

#### 3.6.1. Photocatalytic degradation mechanism

Based on the intermediates detected, possible pathways of toluene degradation were proposed as shown in Fig. 10. With the irradiation of visible light, CIS is excited to produce photogenic electrons and holes. Due to phenomenal conductivity of carbon nanofibers, the conduction band of CIS is excited to generate photogenerated electrons and transfer to carbon nanofibers. Moreover, the close combination of CIS and CNFS provides a good transmission platform for photogenerated carriers. Therefore, the photogenerated electron-hole pairs can be separated effectively. In the process of toluene degradation, the holes in the CIS valency band oxidize  $\text{H}_2\text{O}(\text{g})$  molecules to  $\text{O}_2$  and  $\text{H}^+$ , then photogenerated electrons on carbon nanofibers combine with  $\text{O}_2$  to

produces  $O_2^{\bullet -}$  (superoxide radical) with strong redox and further react with water molecules to generate  $OH^{\bullet}$  (hydroxyl radical). According to the above results, the transport and degradation mechanism of the photo-generated carrier of CIS/CNFs composite photocatalyst can be described by the following equation:



According to the stoichiometry, one oxygen molecule reacts with three electron holes and two water molecules to produce four  $OH^{\bullet}$  [9, 39]. Toluene is then oxidized to carbon dioxide and water [40-42].

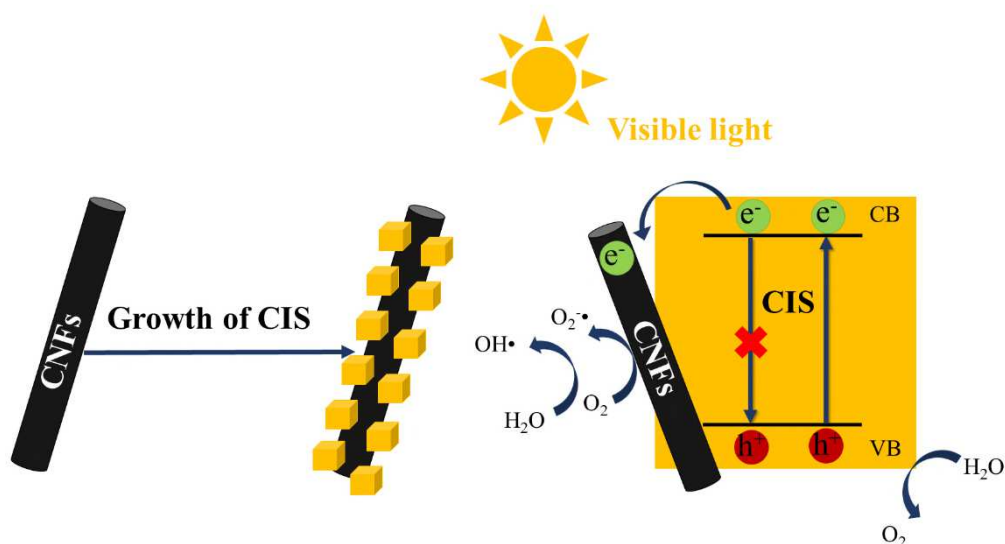


Fig. 10 Visible light photocatalysis mechanism of CIS/CNFs composite

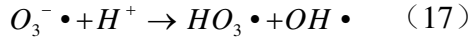
### 3.6.2. Possible mechanism for ozone-enhanced photocatalysis

The above experimental results proved that during ozone into the PCO system not only improves the removal efficiency of toluene, but also contributes significantly to the mineralization of toluene. At present, the mainstream view believes that its mechanism is associated the synergistic effect of mutual influence [13]. It is believed that  $O\bullet$  and  $OH\bullet$  played major roles in  $O_3$ -PCO system and occur in CIS/CNFs+ $O_3$  and CIS/CNFs +Vis+ $O_3$ .

In the CIS/CNFs+ $O_3$  process, oxygen molecules react with active sites of the photocatalyst,  $O\bullet$  reacts further with water vapor in the gas phase, and one ozone produces two  $OH\bullet$ . At the same time, as a high electron affinity gas, ozone is easier to capture the electrons generated by light, thus reducing the electron-hole pair recombination rate and accelerating the formation of  $OH\bullet$  [43].



With the irradiation of visible light, CIS is excited to produce photogenic electrons and holes in the CIS/CNFs +Vis+ $O_3$  process. At the same time,  $O_2^{\bullet-}$ ,  $OH^-$ , and  $H^+$  are generated. The photogenic electrons react with ozone to generate  $O_3^-$ , which combines with  $H^+$  to generate  $HO_3\bullet$  and further decomposes to  $OH\bullet$ . Subsequently, ozone reacts with the  $OH^-$  generated in photocatalysis to form  $O_3^- \bullet$  and hydrogen peroxy radical ( $HO_2\bullet$ ), which further produces the highly oxidizing superoxide radical ( $O_2^{\bullet-}$ ), and the above process is repeated.



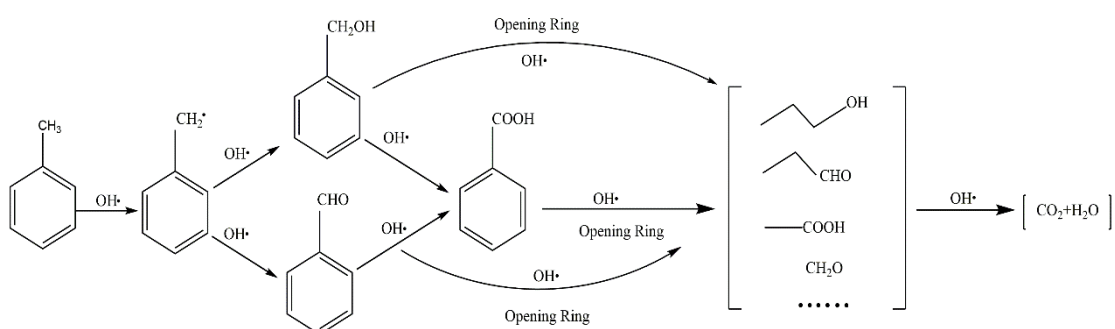
The effect of humidity on toluene removal achieved with O<sub>3</sub>-PCO indicate that water molecules play an important role in the initial stage of O<sub>3</sub>-PCO chain reaction. However, in the case of high humidity, ozone molecules and water molecules compete for adsorption sites on the catalyst surface, which is not conducive for toluene removal [44].

In summary, two powerful oxidants which OH• and O•, are involved two ways in the degradation of toluene.

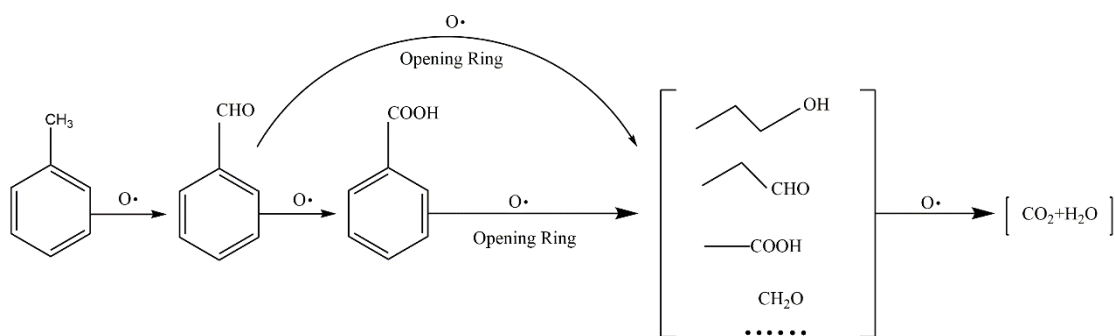
(1) When OH• is the main oxidant oxidizing for toluene, OH• was H-abstraction from methyl resulting in the production of benzyl alcohol and benzaldehyde, which is further attacked by OH• oxidant and then the aromatic ring opens, gradually forming CO<sub>2</sub> and H<sub>2</sub>O. In this pathway (Fig. 11(a)), byproducts such as formic acid and benzaldehyde are abundant [45, 46].

(2) The primary pathway of toluene oxidation by O• is via abstraction of two H atoms from methyl to directly produce benzaldehyde which is then opened after being continuously attacked by O•, and then reacts similar to OH• [13, 47]. In this path, the intermediate product is only benzaldehyde (Fig. 11(b)). Compared with OH•, the reaction steps with O• as oxidant are shorter, the intermediates are fewer, and the reaction is faster. As will be readily seen, compared with PCO reaction, O<sub>3</sub>-PCO process produces more oxidants and less byproducts.

The above analysis is based on the previous studies and analyses of the by-products attached to the photocatalyst surface. The above processes are all based on the degradation of toluene under the ideal state. We observed some intermediates using GC-MS, as shown in Fig. S5. However, in the actual detection of intermediate products, additional intermediate products were detected, among which the characteristic peaks of benzaldehyde, phenol and benzoic acid appeared at 8.481, 15.254 and 17.326 min, respectively. Meanwhile, the undecomposed toluene characteristic peak appears at 6 min [48]. Therefore, according to ideal state and the actual observation, we summarized reactions leading to toluene degradation in O<sub>3</sub>-PCO system (Fig. 11).



(A) OH• degradation process



(B) O• degradation process

Fig. 11 Possible mechanism for ozone-enhanced photocatalysis of toluene

Therefore, when the above multiple reactions are combined on the surface of photocatalyst as a more powerful oxidant, ozone greatly increases the amount and rate of OH• and O• formation. Moreover, due to the high electron affinity of ozone, it is easier to capture the electrons that have transited to the conduction band after being exposed to visible light, which means that it is easier to decrease the recombination rate of the electron-hole pairs by scavenging photo-induced electrons. As a result, the efficiency of photocatalytic oxidation toward toluene was improved.

#### **4. Conclusions**

In this study, CdIn<sub>2</sub>S<sub>4</sub>/CNFs were synthesized by a simple hydrothermal method, and the composite materials were irradiated by visible light to degrade toluene, besides taking advantage of ozone to enhance degradation efficiency. The successful preparation of CIS/CNFs composites by hydrothermal method was confirmed by XRD and XPS. Compared with CIS nanoparticles, CIS/CNFs composite materials have a higher specific surface area, leading to CIS/CNFs having significant adsorption capacity. The 3D conductive network formed by CIS nanoparticles and carbon nanofibers was closely combined as shown in SEM and TEM. The results showed that CNFs (about 300 nm in diameter) were well connected with CIS to form a 3D conductive network and the CIS with 100 nm in average particle size were uniformly grown onto the surface of CNFs. Under visible light irradiation, the degradation efficiency of toluene achieved with CIS doped with 3% CNFs is 86%. For the purpose of further improving the efficiency, with the

introduction of 200 ppm ozone, the toluene removal efficiency is increased to 95%. Ozone catalytic oxidation has significantly improved toluene removal efficiency and mineralization rate. Meanwhile, after ten times of repeated use, the photocatalytic activity decreased by only 3.42%, proving that the CIS/CNFs composite material has excellent repeated use performance. Through photocurrent and PL spectrum analysis, it is found that the CIS/CNFs composite material has a better photoelectron and hole separation rate than CIS nanoparticles. The results show that the CIS/CNFs composite material has higher quantum efficiency and improved its photocatalytic activity. Based on the intermediate by-products measured by GC-MS, the mechanism of ozone catalytic oxidation of toluene was proposed. The results show that ozone can generate more hydroxyl and oxygen radicals, thereby further reduced the recombination of electron-hole pairs. Increasing the ozone consumption rate and completely degrade the remaining ozone needs further investigation in subsequence. This study provides a new strategy to prepare the CIS/CNFs composites with high photocatalytic activity and excellent recyclable performance.

#### Abbreviations list

CIS: CdIn<sub>2</sub>S<sub>4</sub>;

CNFs: carbon nanofibers;

O<sub>3</sub>-PCO: Ozone-enhanced photocatalytic oxidation;

3D: three-dimensional;

VOCs: volatile organic compounds;

VIS: visible light;

XRD: X-ray diffraction;

SEM: Scanning electron microscope;

XPS: X-ray photoelectron spectroscopy;

TEM: transmission electron microscopy;

HRTEM: High-resolution transmission electron microscopy;

PL: Photoluminescence;

GC-MS: gas chromatography coupled with mass spectrometer;

## Support information

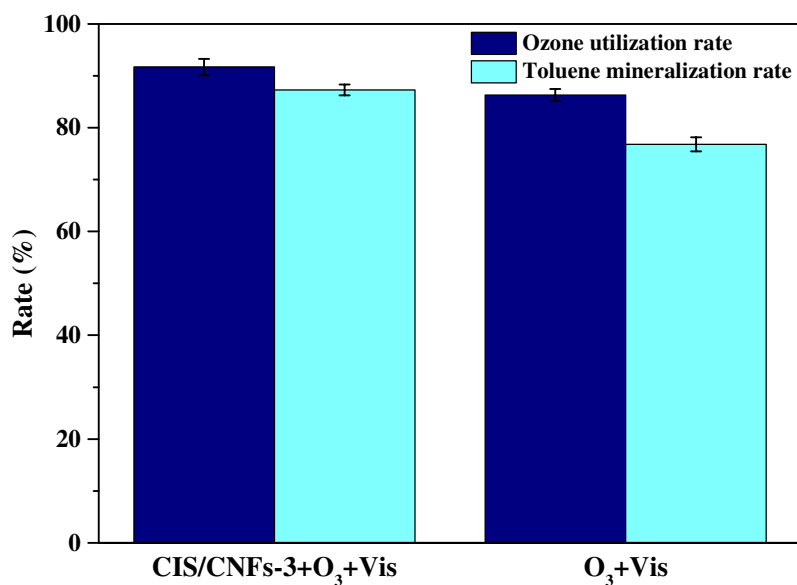


Fig. S1 Ozone utilization and mineralization rates of toluene achieved with two processes.

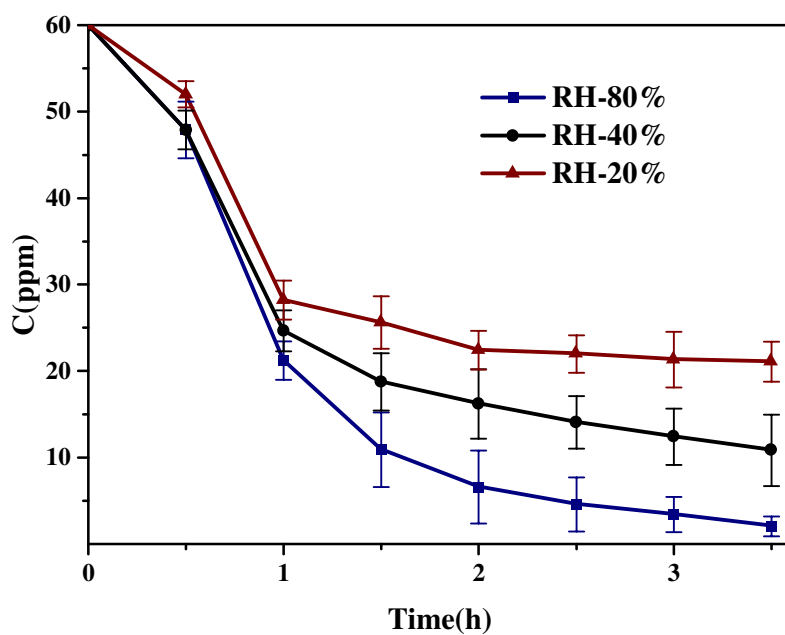


Fig. S2 Influence of relative humidity on toluene removal achieved with.

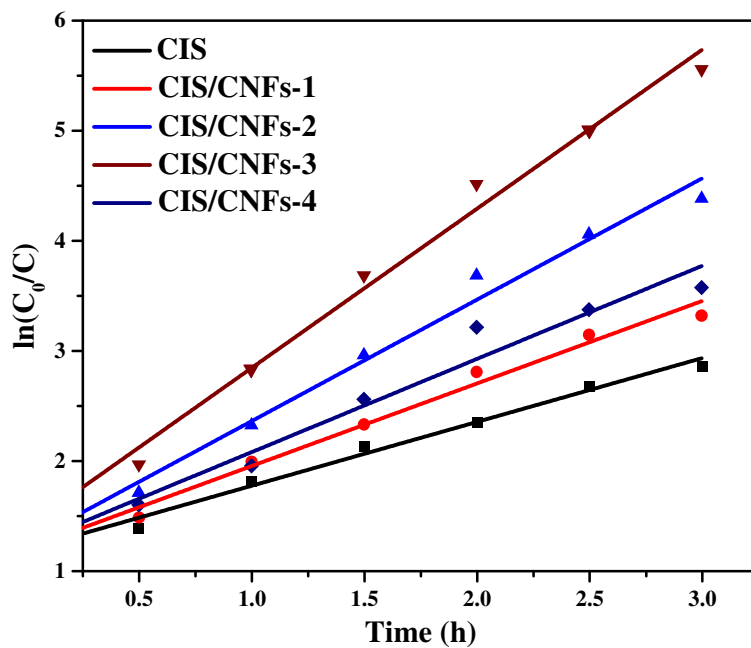


Fig. S3 Photodegradation rate of toluene achieved with CIS and different CNFs doping (assuming that the reaction follows the pseudo-first-order kinetic model)

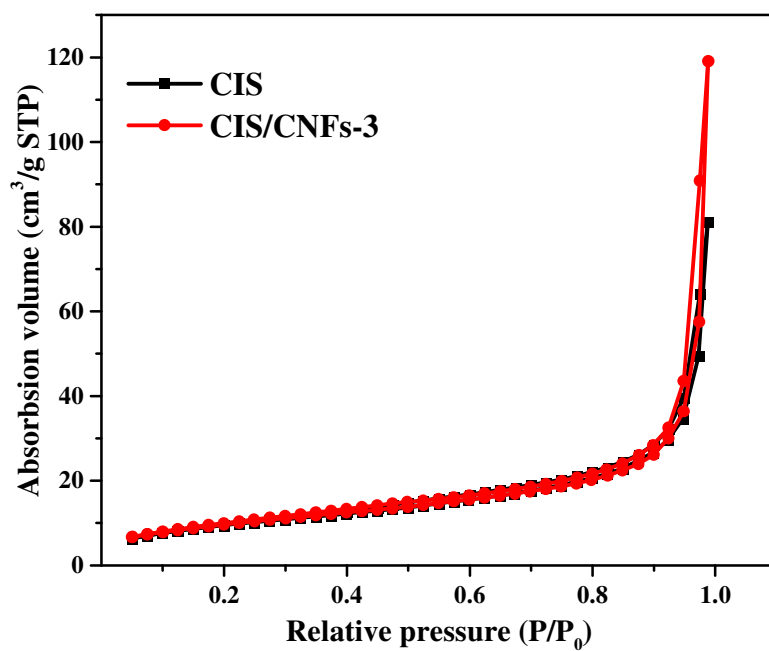


Fig. S4 N<sub>2</sub> adsorption-desorption isotherms of CIS and CIS/CNFs-3.

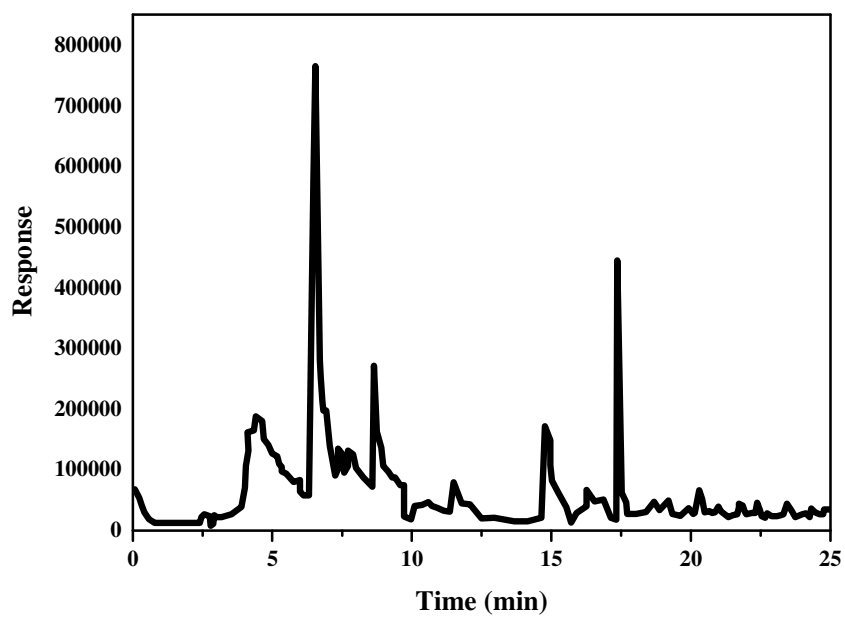


Fig. S5 Analysis of intermediate products by GC-MS

## Declarations

### Competing interests

#### Declaration of interests

The authors declare that they have no known competing financial interests or personal relationships that could have appeared to influence the work reported in this paper.

The authors declare the following financial interests/personal relationships which may be considered as potential competing interests:

*Tung-Peean Chang*  
*Rama R. L. V. S.*

**Availability of data and materials**

All data generated or analyzed during this study are included in this published article [and its supplementary information files]

**Competing interests**

The authors declare they have no competing interests.

**Acknowledgment**

Not applicable

**Funding**

Not applicable

**Authors' contributions**

Runyu Liu: Conceptualization, Resources, Formal analysis Data curation, Writing – original draft, Writing - review & editing.

Minh Man Trinh: Project administration, Supervision, Writing - review & editing.

Moo Been Chang: Conceptualization, Methodology, Supervision, Writing - review & editing.

## References

- [1] Alberici RM, Jardim WF. Photocatalytic destruction of VOCs in the gas-phase using titanium dioxide. *Appl. Catal. B* 1997;14(1-2):55-68.
- [2] Atkinson R. Atmospheric chemistry of VOCs and NOx. *Atmospheric Environ.* 2000;34(12-14):2063-101.
- [3] Van Durme J, Dewulf J, Sysmans W, Leys C, Van Langenhove H. Abatement and degradation pathways of toluene in indoor air by positive corona discharge. *Chemosphere* 2007;68(10):1821-9.
- [4] Yue Z, Vakili A, Wang J. Activated carbon fibers from meltblown isotropic pitch fiber webs for vapor phase adsorption of volatile organic compounds. *Chem. Eng. J.* 2017;330:183-90.
- [5] Shi L, Huang W. Sensitivity analysis and optimization for gasoline vapor condensation recovery. *Process Saf. Environ. Prot* 2014;92(6):807-14.
- [6] Choi B-S, Yi J. Simulation and optimization on the regenerative thermal oxidation of volatile organic compounds. *Chem. Eng. J* 2000;76(2):103-14.
- [7] Vandembroucke AM, Morent R, De Geyter N, Leys C. Non-thermal plasmas for non-catalytic and catalytic VOC abatement. *J Hazard Mater* 2011;195:30-54.
- [8] Ye H, Liu Y, Chen S, Wang H, Liu Z, Wu Z. Synergetic effect between non-thermal plasma and photocatalytic oxidation on the degradation of gas-phase toluene: Role of ozone. *Chin. J. Catal* 2019;40(5):631-7.
- [9] Yu K, Lee G. Decomposition of gas-phase toluene by the combination of ozone and photocatalytic oxidation process (TiO<sub>2</sub>/UV, TiO<sub>2</sub>/UV/O<sub>3</sub>, and UV/O<sub>3</sub>). *Appl. Catal. B* 2007;75(1-2):29-38.
- [10] Shu Y, Ji J, Xu Y, Deng J, Huang H, He M, et al. Promotional role of Mn doping on catalytic oxidation of VOCs over mesoporous TiO<sub>2</sub> under vacuum ultraviolet (VUV) irradiation. *Appl. Catal. B* 2018;220:78-87.
- [11] Mamaghani AH, Haghghat F, Lee CS. Photocatalytic oxidation technology for indoor environment air purification: the state-of-the-art. *Appl. Catal. B* 2017;203:247-69.
- [12] Debono O, Hequet V, Le Coq L, Locoge N, Thevenet F. VOC ternary mixture effect on ppb level photocatalytic oxidation: Removal kinetic, reaction intermediates and mineralization. *Appl. Catal. B* 2017;218:359-69.
- [13] Huang H, Li W. Destruction of toluene by ozone-enhanced photocatalysis: Performance and mechanism. *Appl. Catal. B* 2011;102(3-4):449-53.
- [14] Bariki R, Majhi D, Das K, Behera A, Mishra BG. Facile synthesis and photocatalytic efficacy of UiO-66/CdIn<sub>2</sub>S<sub>4</sub> nanocomposites with flowerlike 3D-microspheres towards aqueous phase decontamination of triclosan and H<sub>2</sub> evolution. *Appl. Catal. B* 2020;270.
- [15] Qiu F, Han Z, Peterson JJ, Odoi MY, Sowers KL, Krauss TD. Photocatalytic hydrogen generation by CdSe/CdS nanoparticles. *Nano Lett.* 2016;16(9):5347-52.
- [16] Liang Q, Cui S, Liu C, Xu S, Yao C, Li Z. Construction of CdS@UIO-66-NH<sub>2</sub> core-shell nanorods for enhanced photocatalytic activity with excellent photostability. *J Colloid Interface Sci* 2018;524:379-87.
- [17] Li G, Wang B, Zhang J, Wang R, Liu H. Rational construction of a direct Z-scheme g-C<sub>3</sub>N<sub>4</sub>/CdS photocatalyst with enhanced visible light photocatalytic activity and degradation of erythromycin and tetracycline. *Appl. Surf. Sci.* 2019;478:1056-64.

- [18] Chu J, Han X, Yu Z, Du Y, Song B, Xu P. Highly efficient visible-light-driven photocatalytic hydrogen production on CdS/Cu<sub>7</sub>S<sub>4</sub>/g-C<sub>3</sub>N<sub>4</sub> ternary heterostructures. *ACS Appl. Mater. Interfaces* 2018;10(24):20404-11.
- [19] Yim W, Fan A, Stofko E. Preparation and properties of II-Ln<sub>2</sub>-S<sub>4</sub> ternary sulfides. *J. Electrochem. Soc.* 1973;120(3):441.
- [20] Zhang P, Shao C, Zhang Z, Zhang M, Mu J, Guo Z, et al. In situ assembly of well-dispersed Ag nanoparticles (AgNPs) on electrospun carbon nanofibers (CNFs) for catalytic reduction of 4-nitrophenol. *Nanoscale* 2011;3(8):3357-63.
- [21] Zhang P, Shao C, Li X, Zhang M, Zhang X, Su C, et al. An electron-rich free-standing carbon@Au core-shell nanofiber network as a highly active and recyclable catalyst for the reduction of 4-nitrophenol. *Phys. Chem. Chem. Phys.* 2013;15(25):10453-8.
- [22] Peng L, Hu L, Fang X. Energy harvesting for nanostructured self-powered photodetectors. *Adv. Funct. Mater.* 2014;24(18):2591-610.
- [23] Zhang M, Shao C, Mu J, Zhang Z, Guo Z, Zhang P, et al. One-dimensional Bi<sub>2</sub>MoO<sub>6</sub>/TiO<sub>2</sub> hierarchical heterostructures with enhanced photocatalytic activity. *CrystEngComm* 2012;14(2):605-12.
- [24] Zhang X, Shao C, Li X, Lu N, Wang K, Miao F, et al. In<sub>2</sub>S<sub>3</sub>/carbon nanofibers/Au ternary synergetic system: hierarchical assembly and enhanced visible-light photocatalytic activity. *J Hazard Mater* 2015;283:599-607.
- [25] Wang Y, Sunarso J, Chen G, Zhao S, Liu Z, Wei Y. Photocatalytic activity of novel Bi<sub>2</sub>WO<sub>6</sub>/CNFs composite synthesized via two distinct solvothermal steps. *Mater. Lett.* 2017;197:102-5.
- [26] Zhang Y, Shao C, Li X, Lu N, Zhang M, Zhang P, et al. Controllable synthesis and enhanced visible photocatalytic degradation performances of Bi<sub>2</sub>WO<sub>6</sub>-carbon nanofibers heteroarchitectures. *J. Sol-Gel Sci. Technol.* 2014;70(1):149-58.
- [27] Li W, Zeng L, Yang Z, Gu L, Wang J, Liu X, et al. Free-standing and binder-free sodium-ion electrodes with ultralong cycle life and high rate performance based on porous carbon nanofibers. *Nanoscale* 2014;6(2):693-8.
- [28] Li X, Ma J, Yang L, He G, Zhang C, Zhang R, et al. Oxygen vacancies induced by transition metal doping in gamma-MnO<sub>2</sub> for highly efficient ozone decomposition. *Environ. Sci. Technol.* 2018;52(21):12685-96.
- [29] Li X, Ma J, Zhang C, Zhang R, He H. Detrimental role of residual surface acid ions on ozone decomposition over Ce-modified gamma-MnO<sub>2</sub> under humid conditions. *J Environ Sci (China)* 2020;91:43-53.
- [30] Xie Y, Yu Y, Gong X, Guo Y, Guo Y, Wang Y, et al. Effect of the crystal plane figure on the catalytic performance of MnO<sub>2</sub> for the total oxidation of propane. *CrystEngComm* 2015;17(15):3005-14.
- [31] Radmilovic V, Gasteiger H, Ross P. Structure and chemical composition of a supported Pt-Ru electrocatalyst for methanol oxidation. *J. Catal.* 1995;154(1):98-106.
- [32] Zhu SR, Liu PF, Wu MK, Zhao WN, Li GC, Tao K, et al. Enhanced photocatalytic performance of BiOBr/NH<sub>2</sub>-MIL-125(Ti) composite for dye degradation under visible light. *Dalton Trans.* 2016;45(43):17521-9.
- [33] Yang Z, Tong X, Feng J, He S, Fu M, Niu X, et al. Flower-like BiOBr/UiO-66-NH<sub>2</sub> nanosphere with improved photocatalytic property for norfloxacin removal. *Chemosphere* 2019;220:98-106.

- [34] Chen H, Jiang G, Yu W, Liu D, Liu Y, Li L, et al. Electrospun carbon nanofibers coated with urchin-like  $\text{ZnCo}_2\text{O}_4$  nanosheets as a flexible electrode material. *J. Mater. Chem. A* 2016;4(16):5958-64.
- [35] Wang J, Yang T, He R, Xue K, Sun R, Wang W, et al. Silver-loaded  $\text{In}_2\text{S}_3\text{-CdIn}_2\text{S}_4\text{@X}$  ( $\text{X}=\text{Ag}$ ,  $\text{Ag}_3\text{PO}_4$ ,  $\text{AgI}$ ) ternary heterostructure nanotubes treated by electron beam irradiation with enhanced photocatalytic activity. *Sci. Total Environ.* 2019;695:133884.
- [36] Bariki R, Majhi D, Das K, Behera A, Mishra BG. Facile synthesis and photocatalytic efficacy of  $\text{UiO-66/CdIn}_2\text{S}_4$  nanocomposites with flowerlike 3D-microspheres towards aqueous phase decontamination of triclosan and  $\text{H}_2$  evolution. *Appl. Catal. B* 2020;270.
- [37] Zhou H, Wen Z, Liu J, Ke J, Duan X, Wang S. Z-scheme plasmonic Ag decorated  $\text{WO}_3/\text{Bi}_2\text{WO}_6$  hybrids for enhanced photocatalytic abatement of chlorinated-VOCs under solar light irradiation. *Appl. Catal. B* 2019;242:76-84.
- [38] Zhang B, Shi H, Hu X, Wang Y, Liu E, Fan J. A novel S-scheme  $\text{MoS}_2/\text{CdIn}_2\text{S}_4$  flower-like heterojunctions with enhanced photocatalytic degradation and  $\text{H}_2$  evolution activity. *J. Phys. D Appl. Phys.* 2020;53(20).
- [39] Pichat P, Disdier J, Hoang-Van C, Mas D, Goutailler G, Gaysse C. Purification/deodorization of indoor air and gaseous effluents by  $\text{TiO}_2$  photocatalysis. *Catal. Today* 2000;63(2-4):363-9.
- [40] Wenderich K, Mul G. Methods, mechanism, and applications of photodeposition in photocatalysis: a review. *Chem Rev* 2016;116(23):14587-619.
- [41] Li X, Yu J, Wageh S, Al Ghamdi AA, Xie J. Graphene in photocatalysis: a review. *Small* 2016;12(48):6640-96.
- [42] Hou W, Cronin SB. A review of surface plasmon resonance-enhanced photocatalysis. *Adv. Funct. Mater.* 2013;23(13):1612-9.
- [43] Maciucă A, Batiot-Dupeyrat C, Tatibouët J-M. Synergetic effect by coupling photocatalysis with plasma for low VOCs concentration removal from air. *Appl. Catal. B* 2012;125:432-8.
- [44] Han W, Zhang P, Zhu W, Yin J, Li L. Photocatalysis of p-chlorobenzoic acid in aqueous solution under irradiation of 254 nm and 185 nm UV light. *Water Res.* 2004;38(19):4197-203.
- [45] Frankcombe TJ, Smith SC. OH-initiated oxidation of toluene. 1. Quantum chemistry investigation of the reaction path. *J. Phys. Chem. A* 2007;111(19):3686-90.
- [46] Sleiman M, Conchon P, Ferronato C, Chovelon J-M. Photocatalytic oxidation of toluene at indoor air levels (ppbv): Towards a better assessment of conversion, reaction intermediates and mineralization. *Appl. Catal. B* 2009;86(3-4):159-65.
- [47] Einaga H, Futamura S. Catalytic oxidation of benzene with ozone over alumina-supported manganese oxides. *J. Catal.* 2004;227(2):304-12.
- [48] Zhang M, Liu X, Zeng X, Wang M, Shen J, Liu R. Photocatalytic degradation of toluene by  $\text{In}_2\text{S}_3/\text{g-C}_3\text{N}_4$  heterojunctions. *Chem. Phys. Lett.: X* 2020;7.
- [49] Sun R, Shi Q, Zhang M, Xie L, Chen J, Yang X, et al. Enhanced photocatalytic oxidation of toluene with a coral-like direct Z-scheme  $\text{BiVO}_4/\text{g-C}_3\text{N}_4$  photocatalyst. *J. Alloys Compd.* 2017;714:619-26.
- [50] Liu Y, Xie C, Li J, Zou T, Zeng D. New insights into the relationship between photocatalytic activity and photocurrent of  $\text{TiO}_2/\text{WO}_3$  nanocomposite. *Appl Catal A Gen* 2012;433-434:81-7.
- [51] Liu J, Wang P, Qu W, Li H, Shi L, Zhang D. Nanodiamond-decorated ZnO catalysts with enhanced photocorrosion-resistance for photocatalytic degradation of gaseous toluene. *Appl. Catal. B* 2019;257.

Table 1. Comparison of photocatalytic decomposition of toluene obtained in this study and literature.

Catalyst	C <sub>in</sub> (ppm)	Removal efficiency (%)	Ref
CIS/CNFs-3	60	86	This study
BiVO <sub>4</sub> / g-C <sub>3</sub> N <sub>4</sub>	25	68.2	[49]
TiO <sub>2</sub> /WO <sub>3</sub>	50	74	[50]
ZnO	50	70	[51]
30%-In <sub>2</sub> S <sub>3</sub> /g-C <sub>3</sub> N <sub>4</sub>	60	80	[48]

C<sub>in</sub>: inlet concentration of toluene.